Mon. Not. R. Astron. Soc. **000**, 1–7 (2006)   Printed 1 February 2008   (MN LaTeX style file v2.2)

arXiv:0706.2564v1 [astro-ph] 18 Jun 2007

Hubble Space Telescope far-ultraviolet imaging of the jet in 3C 273: a common emission component from optical to X-rays*

Sebastian Jester,[1]† Klaus Meisenheimer[1], André R. Martel,[2] Eric S. Perlman[3]
and William B. Sparks[4]
[1]*Max-Planck-Institut für Astronomie, Königstuhl 17, 69117 Heidelberg, Germany*
[2]*Department of Physics & Astronomy, The Johns Hopkins University, 3400 N. Charles Street, Baltimore, MD 21218, USA*
[3]*Physics and Space Sciences Department, Florida Institute of Technology, 150 West University Boulevard, Melbourne, FL 32901, USA*
[4]*Space Telescope Science Institute, 3700 San Martin Drive, Baltimore, MD 21218, USA*

Accepted 2007 June 17. Received 2007 June 12; in original form 2007 March 23

ABSTRACT
We present far-ultraviolet (UV) observations at ~ 150 nm of the jet of the quasar 3C 273 obtained with the Advanced Camera for Survey's Solar Blind Channel (ACS/SBC) on board the *Hubble Space Telescope*. While the jet morphology is very similar to that in the optical and near-ultraviolet, the spectral energy distributions (SEDs) of the jet's sub-regions show an upturn in νf_ν at 150 nm compared to 300 nm everywhere in the jet. Moreover, the 150 nm flux is compatible with extrapolating the X-ray power-law down to the ultra-violet region. This constitutes strong support for a common origin of the jet's far-UV and X-ray emission. It implies that even a substantial fraction of the *visible light* in the X-ray brightest parts of the jet arises from the same spectral component as the X-rays, as had been suggested earlier based on *Spitzer Space Telescope* observations. We argue that the identification of this UV/X-ray component opens up the possibility to establish the synchrotron origin of the X-ray emission by *optical* polarimetry.

Key words: quasars: individual: 3C273 – galaxies:active – galaxies:jets – radiation mechanisms: non-thermal – acceleration of particles

1 INTRODUCTION

The launch of the *Chandra X-ray Observatory* has led to an order-of-magnitude increase in the number of X-ray detections from extragalactic jets (*e.g.*, Worrall et al. 2001; Sambruna et al. 2002, 2004; Marshall et al. 2005; H. Marshall et al. *in prep.*). There is currently a very active debate about the origin of X-ray emission from many high-power jets, in which the X-ray and radio emission cannot be explained by a single spectral component. The X-rays could be due to beamed inverse-Compton (IC) scattering of cosmic microwave background (CMB) photons, or due to synchrotron emission from a second electron population (Tavecchio et al. 2000; Celotti, Ghisellini & Chiaberge 2001; Stawarz et al. 2004; Hardcastle 2006; Harris & Krawczynski 2006); synchrotron self-Compton (SSC) emission from electrons in an equipartition magnetic field can usually account for the X-ray emission from *hot spots* at the ends of jets (see Harris & Krawczynski 2006), but in the jets themselves, SSC is only viable if the total energy density is dominated by relativistic electrons at the level of 99.99% or more, and we will not consider it further here.

One debated case is the jet in 3C273, where data from *ROSAT* and the first *Chandra* observations had left the X-ray emission mechanism unclear (Röser et al. 2000; Marshall et al. 2001; Sambruna et al. 2001). In Jester et al. (2006), we presented deeper Chandra observations of this jet and found that the X-ray spectra are softer than the radio spectra in nearly all parts of the jet, ruling out the simplest one-zone beamed IC-CMB (BIC) models. A BIC model could still work if the jet flow has a spine + sheath (or otherwise inhomogeneous) structure, but we found synchrotron emission from a high-energy electron population to be a more plausible scenario, as velocity shear is very likely to be present and is capable of accelerating particles (Stawarz & Ostrowski 2002; Rieger & Duffy 2004).

Evidence for synchrotron X-ray emission in this jet has also come from an analysis of the overall SED shape. Jester et al. (2002) demonstrated that all parts of the jet show a UV excess above a simple synchrotron spectrum fitted to the radio, infrared and optical data, and suggested that part of the optical/UV emission might be due to the same emission component as the jet's X-rays. We there-

---

* Based on observations made with the NASA/ESA Hubble Space Telescope, obtained at the Space Telescope Science Institute, which is operated by the Association of Universities for Research in Astronomy, Inc., under NASA contract NAS 5-26555. These observations are associated with HST program GO-9814

† E-mail: jester@mpia.de; this work was begun at the Particle Astrophysics Center, Fermilab, Batavia, IL 60510, USA

Table 1. Observation log for new ACS/SBC data. All exposures used filter `F150LP`.

Target	Dataset name	Start time UT	Exp. time s
J122903+020318	J8P001010	04/08/2004 23:13:47	900
3C273-JET	J8P001TSQ	04/08/2004 23:32:12	1600
3C273-JET	J8P001020	05/08/2004 00:45:39	2800
3C273-JET	J8P001030	05/08/2004 02:21:37	2800

fore proposed to image the jet at 150 nm, the shortest UV wavelength accessible with the HST, and present the results here.

In the meantime, Uchiyama et al. (2006) had analysed Spitzer images at 3.6 and 5.8 μm. Surprisingly, they found that the *Spitzer* fluxes of the first two bright knots A and B1 lie well above the commonly assumed power-law interpolation between radio and optical/UV. This indicates that the optical/UV emission is already dominated by the X-ray component, as suspected by Jester et al. (2002). Our new results demonstrate that the emission at 150 nm is more closely related to the X-ray than to the radio/IR emission component.

The plan of this paper is as follows: Section 2 describes the observations and data reduction. In Section 3, we present the resulting image and SEDs including the new 150 nm data point. Section 4 discusses the implications of the new data for the emission mechanisms and jet structure.

2 OBSERVATIONS AND DATA REDUCTION

The Advanced Camera for Surveys (ACS) Solar Blind Channel (SBC) UV detector was used to image the jet in 3C 273 through filter `F150LP`. This filter blocks out geocoronal Lyman-α emission and therefore leads to a substantially higher signal-to-noise ratio than broader filters that extend to shorter wavelengths. The total exposure time spent on the jet was 7200 s. Since the quasar is too bright in the UV to be imaged with the SBC, we could not use it as an astrometric reference point. Therefore, we used 900 s of our allocated time to image a nearby star (Star G in Röser & Meisenheimer 1991) as absolute astrometric reference point. Table 1 gives the observation log.

We used the standard pipeline reductions to create flat-fielded images. Due to a pipeline bug, information about hot pixels was not propagated properly to the data quality (DQ) arrays of the flat-fielded images. We set the necessary DQ bits for the hot pixels listed in the appropriate bad-pixel file and then combined all five individual images using the `multidrizzle` task from the `STSDAS` package, with parameter settings taken from the pipeline-generated `mdriztab` table. The `multidrizzle` task corrects for geometric distortion, enabling surface photometry to be performed on the output image. No cosmic-ray rejection was performed, since the SBC is a Multi-Anode Multi-channel Array (MAMA) which is not sensitive to charged particles.

Visual inspection of the combined image showed that there is a sloping background, most likely due to a large-angle scattering wing of the quasar image (the quasar was placed about $7''$ outside the SBC's field of view to avoid violating the SBC's count rate limits). To fit this background, we used a combination of an exponential profile representing the scattering wing and a constant level representing the overall sky background (an exponential by itself, without a constant offset, left systematic residuals). As the total background level is very low, and the relative pixel-to-pixel noise therefore high, the image was smoothed to $0\farcs2$ resolution prior to background subtraction. The smoothed image will also be used for all science analysis.

The absolute pointing of HST data sets can be established only at the level of $1''$ (Pavlovsky et al. 2006, §6.2.2), which is clearly not nearly sufficient for the multi-band multi-telescope analysis of a jet of width $0\farcs7$; however, the absolute roll angle is sufficiently accurate and precise. In principle, it is of course possible to use the brightness peaks of the jet itself to align images at different wavelengths; however, a spectral index map generated with the help of such an alignment method is of limited use, because *features in spectral index maps arise precisely from morphological differences between bands*. In Jester et al. (2001, Appendix A1) we have shown that the alignment of images for the creation of a reliable spectral index map has to be better than 10% of the PSF width, *i.e.*, at the level of 20 mas or better in this case.

As mentioned above, we had planned to use the images of star G for absolute astrometric calibration. However, both simply using the star's position from Röser & Meisenheimer (1991, i.e., ignoring possible proper motions), and correcting of the position using proper motions from the combined SDSS+USNO-B catalogue by Munn et al. (2004) or the UCAC2 catalogue (Zacharias et al. 2004) yielded an alignment that left obvious offsets compared to data taken in other bands. The reason for the offsets is very likely simply an unhelpful combination of random errors in the individual positions and in the proper motions. The coordinates given by Röser & Meisenheimer (1991) were obtained roughly 20 years before the SBC observation; with proper motion random errors of 3 mas/yr, centroiding errors of 10 mas (RMS, total for both coordinates) and an additional contribution from the SBC distortion correction, the total random error could already be $0\farcs1$, or 1/7 of the jet width. This is roughly the magnitude of the observed offsets.

Hence, absolute astrometry with the accuracy and precision required to compute a spectral index map is not possible at present. Therefore, we restrict the analysis to performing integral photometry of the jet knots, as in Jester et al. (2006), for which a visual placement of the photometry apertures is sufficient. The photometry was performed in the same regions shown in Figure 1 of Jester et al. (2006).

3 RESULTS

3.1 Map of surface brightness and photometry of knots

Figure 1 shows a map of the surface brightness of the jet. The morphology and appearance is identical to that at 620 and 300 nm (also see Figures 1 and 2 in Jester et al. 2001). The surface brightness profile continues the trend for the innermost bright knots to become more dominant at higher frequencies, while the outermost knots are more dominant at lower frequencies. However, in a departure from this trend, the broad edge of H3 appears slightly stronger compared to the round feature D2 at 150 nm (peak ratio of about 1.4:1) than at 620 nm (about 1.25:1). The resolution of *Chandra* is not high enough to examine the X-ray morphology at this level of detail.

3.2 Spectral energy distributions

Figure 2 shows SEDs of the jet knots at all presently available wavelengths, with new SBC measurements reported in Table 2.

Table 2. Integrated flux densities of jet regions at 150 nm, and spectral indices. The flux densities are summed over the same regions as in Jester et al. (2006), which extend along position angle 222° over the radial range $r_{\mathrm{in}} \leqslant r < r_{\mathrm{out}}$, and to about $\pm 0\overset{\prime\prime}{.}4$ from the radius vector. Flux densities for all wavelengths are given in Tab. A1. The spectral indices are defined as follows: α_{X}, spectral index within the *Chandra* band from Jester et al. (2006); $\alpha_{150}^{\mathrm{X}}$ spectral index between 1 keV and 150 nm; $\alpha_{\mathrm{radio}}^{\mathrm{IR}}$ spectral index between 1.4 μm and 10 GHz (1.4 μm is HST NICMOS `F140W`, 10 GHz is interpolated from 3 VLA bands, all from Jester et al. 2005).

Region	r_{in} $''$	r_{out} $''$	f_ν nJy	σ_f nJy	$\alpha_{\mathrm{radio}}^{\mathrm{IR}}$	$\sigma(\alpha_{\mathrm{radio}}^{\mathrm{IR}})$	$\alpha_{150}^{\mathrm{X}}$	$\sigma(\alpha_{150}^{\mathrm{X}})$	α_{X}	$\sigma(\alpha_{\mathrm{X}})$
A	11	12.9	46.5	0.54	-0.90	-0.05	-0.78	-0.01	-0.83	0.02
B1	12.9	13.8	10.9	0.25	-0.96	-0.07	-0.83	-0.01	-0.80	0.03
B2	13.8	14.9	20.0	0.33	-0.93	-0.04	-0.88	-0.01	-0.97	0.03
B3	14.9	15.6	3.41	0.14	-0.93	-0.09	-1.00	-0.02	-1.13	0.07
C1	15.6	16.5	4.85	0.16	-0.92	-0.04	-1.01	-0.01	-1.07	0.06
C2	16.5	17.6	6.25	0.18	-0.94	-0.02	-0.98	-0.01	-0.96	0.05
D1	17.6	18.5	5.16	0.17	-0.95	-0.02	-1.00	-0.01	-1.02	0.05
D2H3	18.5	20.0	7.82	0.20	-1.00	-0.01	-1.06	-0.01	-1.04	0.04
H2	20.0	21.1	1.30	0.086	-1.22	-0.00	-1.11	-0.02	-1.27	0.12

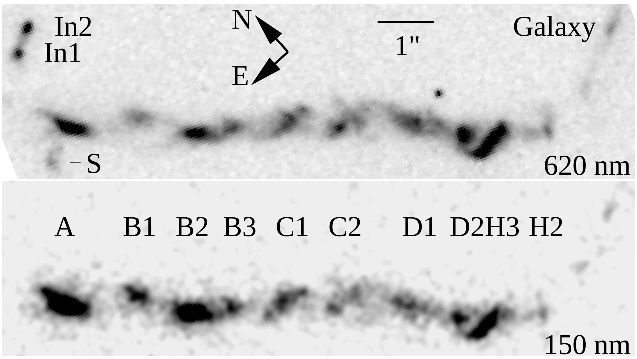

Figure 1. Map of surface brightness (linear grayscale) of 3C273's jet at 150 nm with HST/ACS/SBC/`F150LP` (bottom), and for comparison, at 620 nm with HST/WFPC2/PC1/`F622W` (top; data from Jester et al. 2001). The images have been rotated to place a position angle of 222° along the horizontal. The quasar lies $12''$ to the northeast of knot A. The names of the regions used in the following figures are indicated. On the 620 nm map, S, In1 and In2 label the "optical extensions" that are visible at all wavelengths from 1.4 μm to 300 nm, but not at 150 nm (see section 4.4 for a discussion of the extensions).

Observed fluxes were corrected for galactic extinction using data from Schlegel, Finkbeiner & Davis (1998) and the galactic extinction law as given by Pei (1992). The Spitzer data are taken directly from Uchiyama et al. (2006, Table 1), distributing the reported *Spitzer* flux density of B2+B3 between the individual knots in the same ratio as observed at 1.4μm.

The spatial resolution of *Spitzer* at the wavelengths used, 3.6 and 5.8 μm, is $1\overset{\prime\prime}{.}66$ and $1\overset{\prime\prime}{.}88$, respectively, which is much larger than the jet width and larger than, or comparable to, the knot-to-knot separation. Therefore, the decomposition by Uchiyama et al. (2006) of the *Spitzer* flux profile into individual unresolved components yields measurements that correspond to fluxes taken with apertures extending about $0\overset{\prime\prime}{.}75$ to either side of the jet. To sample the same spatial regions also at the other wavelengths, we have used photometry apertures for the VLA and *HST* data that are considerably larger than those used by Uchiyama et al. (2006) for the VLA and *HST* data. These larger-aperture fluxes are up to 30% higher than those determined by Uchiyama et al. (2006), with smaller differences for the *HST* measurements of the fainter knots. While these differences do not change the overall SED shape appreciably, we judge the resulting SEDs to be more precise.

The salient feature of Figure 2 is that the spectral flux per decade (νf_ν) at 150 nm lies *above* that at 300 nm in all parts of the jet, but on or below the extrapolation of the *Chandra* flux and spectral index.

4 DISCUSSION

4.1 Stronger evidence for a common origin of the jet's far-UV and X-ray flux

In Jester et al. (2002), we reported an optical/UV excess above a synchrotron spectrum with a concave cutoff (in $\log f_\nu$ vs. $\log \nu$). The fact that the excess was largest in the X-ray brightest knot suggested a common origin of the optical/UV excess and the X-rays. Our HST observations at 150 nm were designed to clarify whether the X-ray emission is indeed linked to this excess. Such a link would have been ruled out by finding a drop in the SED from 300 to 150 nm. Instead, the observed rise of the SED at 150 nm compared to 300 nm and the compatibility of the 150 nm flux with an extrapolation of the *Chandra* flux indeed lends strong support to the idea that the UV excess is due to the same emission component as the X-ray emission.

Uchiyama et al. (2006) had argued that there is a contribution to the optical/UV flux from the X-ray component based on the good agreement between the spectral slope of the high-energy power law they fitted from optical to X-rays, and α_{X}, the spectral index within the *Chandra* band. This is confirmed by the even tighter correlation between α_{X} and the far-UV/X-ray spectral index $\alpha_{150}^{\mathrm{X}}$ determined from the SBC and *Chandra* fluxes (Fig. 3a and Tab. 2). These spectral indices are clearly consistent with being equal in B1, C1, C2, D1, and D2H3. Due to its large error bar on α_{X}, the point for in H2 is also compatible with lying on the equality line, while A, B2 and B3 lie below the equality line at higher significance. B3 is the smallest region, with an angular extent similar to the *Chandra* resolution element, and therefore suffers from the largest systematic uncertainties in determining spectral indices and it may be an outlier simply due to these errors. On the other hand, A and B2 stand out from the remainder of the jet as the regions with the strongest X-ray emission, and in the case of A, with an emission peak that

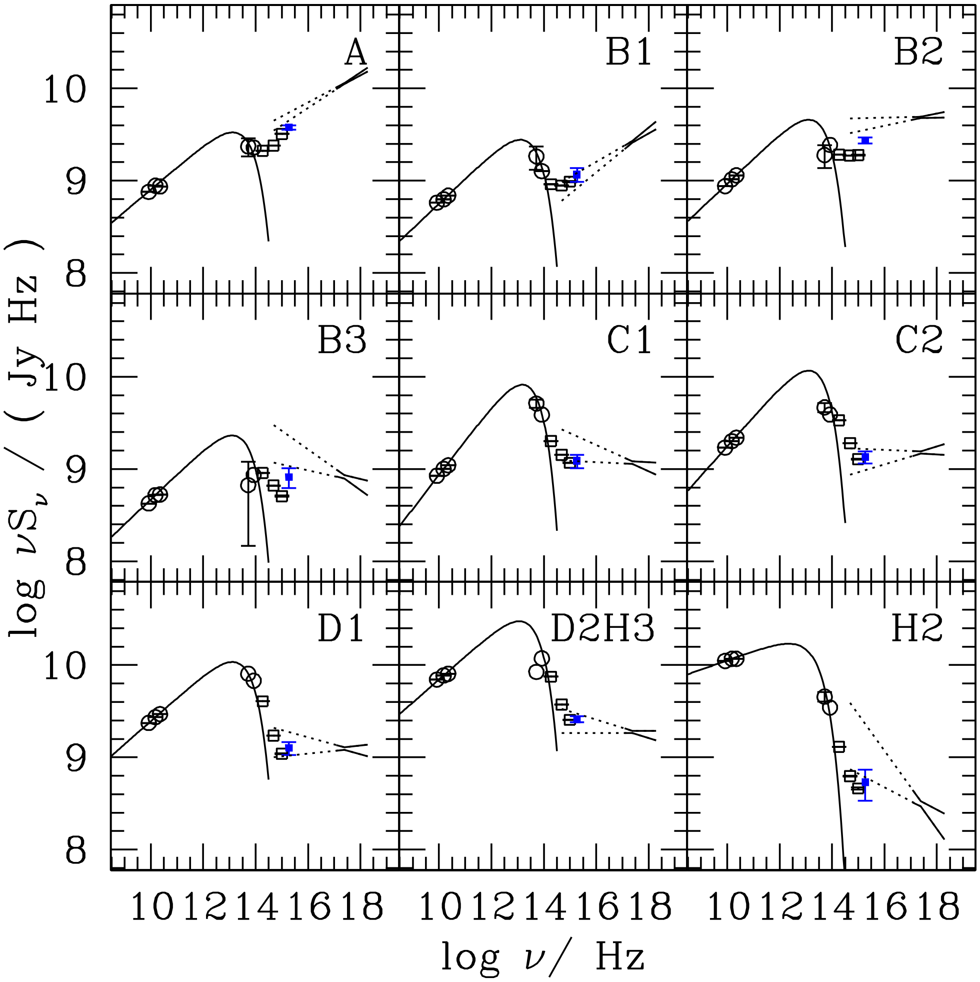

Figure 2. SED of 3C273 jet regions, including VLA, Spitzer, HST and Chandra fluxes listed in Tab. A1. The new SBC data at 150 nm are represented by solid squares (blue in electronic versions); previous HST data by open squares; Spitzer and VLA data by open circles; Chandra data by "bow ties" (solid lines show the observed region, dotted lines the extrapolation into the optical/UV). The solid curves show the an exponential cutoff indicating the likely contribution from the low-frequency component of the spectrum (these are *not* fits, just illustrations, but similar to the curves fitted by Uchiyama et al. 2006). In all parts of the jet, the spectral energy density at 150 nm (2×10^{15} Hz) lies above that at 300 nm (10^{15} Hz), but is compatible with lying on or below an extrapolation of the Chandra flux to lower frequencies. This is strong evidence that the jet emission at 150 nm is predominantly or exclusively due to the same component as the X-rays. In A, B1 and B2, even the *optical* emission is dominated by this component.

is unresolved by Chandra; this again suggests a difference between these bright regions and the remainder of the jet, perhaps the presence of a shock that is responsible for accelerating the X-ray emitting particles.

As pointed out by Katz-Stone, Rudnick & Anderson (1993), a "colour-colour" diagram such as Figure 3a is a powerful diagnostic both of the underlying spectral shape and of the homogeneity of spectral shapes at different locations in the source. The similarity of the spectral indices in Figure 3a implies that the emission from 150 nm up to the *Chandra* band is consistent with being a power law in all parts of the jet (perhaps with a "cut-on", a sharp rise in spectral power density with increasing frequency, in A, B2 and B3, where $\alpha_{\rm X}$ dips below $\alpha^{\rm X}_{150}$). Figure 3b shows that the slope of this power-law tends to decrease outward along the jet, while the spectral index $\alpha^{\rm IR}_{\rm radio}$ from radio to infrared is consistent with a constant out to D1 and drops only further out (the constancy of $\alpha^{\rm IR}_{\rm radio}$ reflects the fact that the radio and IR brightness profiles are similar). In other words, the spectral shape of the low-energy component remains constant (Jester et al. 2001), while that of the high-energy component evolves strongly along the jet.

The new SBC data substantially strengthen the conclusion of Uchiyama et al. (2006) that the jet's far-UV emission is of the same origin as the X-rays; furthermore, in the X-ray brightest regions A, B1 and B2, a large fraction of the emission in the optical/near-UV is already contributed by the same spectral component as the X-rays. It is difficult to quantify this fraction exactly, because it depends sensitively on the detailed shape of the cutoff to the low-energy emission; we estimate this fraction to be above 50% in knots A, B1 and B2, but much less in the remainder of the jet.

The fact that the X-ray:radio ratio drops along the jet in the same way as the X-ray spectral index $\alpha_{\rm X}$ should provide a hint to the origin of the X-ray emitting particles. This behaviour is the opposite of that seen in the so-called *blazar sequence* (Fossati et al. 1998), where a lower X-ray flux goes along with a *harder* X-ray

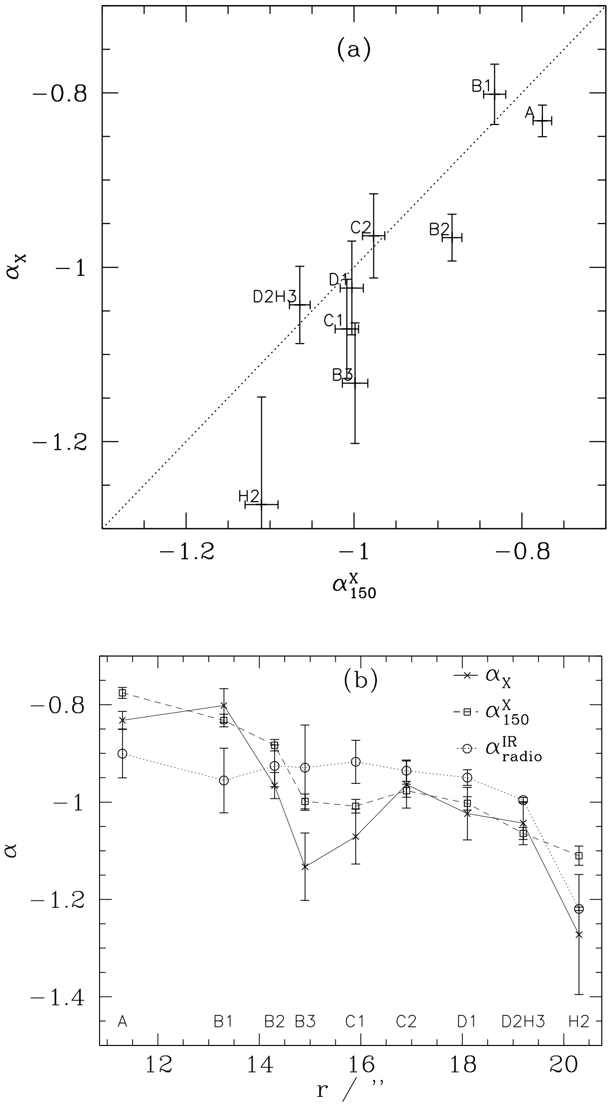

Figure 3. (a) Comparison of α_X, the spectral index within the *Chandra* band, and α^X_{150}, the spectral index between 150 nm and the X-ray flux at 1 keV (corresponding to 1.24 nm and 2.42×10^{17} Hz). The tight correlation is evidence for a common origin of the 150 nm and X-ray emission. The near equality of both spectral indices shows that the UV/X-ray SEDs are consistent with power laws (or power laws with a "cut-on" in the UV region in B2 and B3) whose slopes are evolving along the jet. **(b)** Evolution of spectral indices within the X-ray band (0.5-8 keV, α_X), between 150 nm and X-rays (α^X_{150}) and between radio and near-infrared (1.4 μm, α^{IR}_{radio}) along the jet. Out to $r = 18''$, the observed values of α^{IR}_{radio} are consistent with being constant at $\alpha^{IR}_{radio} = -0.95$, while α_X and α^X_{150} drop in accord.

spectrum. In blazars, this relation is seen as evidence for SSC emission as origin of the X-rays, which then might argue *against* an inverse-Compton origin of the X-rays from this jet.

Instead, we speculate that the softening of the X-ray spectrum arises from re-acceleration of some fraction of the electrons in the high-energy tail of the "low-energy" population. We ascribe the spectral softening to a decrease in the acceleration efficiency that is connected to the increase in the radio:X-ray flux ratio, for example by changes in the average magnetic field strength. As described in Jester et al. (2006), this re-acceleration could occur in a thin shear layer around the main jet flow (with the possible exception of A and perhaps B2, which show evidence for more concentrated X-ray emission than the remainder of the jet). The variations in radio:X-ray ratio would be caused both by the decreasing acceleration efficiency, and by variations in the fraction of high-energy electrons that are transferred from the radio/optically emitting part of the flow into the re-acceleration region. Thus, we consider the "high-energy" population to be generated by re-acceleration of electrons initially in the "low-energy" population and escaping into the re-acceleration region.

Because of the significant contribution of the high-energy spectral component to the jet flux in the visible wavelength range, we argue below that it is possible to establish the emission mechanism of the jet's *X-rays* by performing *optical* polarimetry. As this is the first jet to be observed at such short ultraviolet wavelengths, it is presently not known whether the same is true for other high-power radio/X-ray jets, though Spitzer observations of PKS 1136−135 suggest a similar SED in its knot A (Uchiyama et al. 2007).

4.2 Future observations: optical polarimetry as diagnostic of the X-ray emission mechanism

Y. Uchiyama & P. Coppi (*in prep.*) have considered the polarisation of IC-CMB emission by electrons in a jet with high bulk Lorentz factor. We summarize their findings as follows: the emission from non-relativistic electrons has a linear polarisation, because the bulk motion of the jet makes the CMB emission anisotropic in the jet frame, which fixes the scattering geometry and therefore leads to a net polarisation. However, electrons with jet-frame Lorentz factors comparable to, or greater than, the bulk Lorentz factor can scatter photons from a range of directions into the observer's line of sight, so that the polarisation is lowered progressively. In the case of ultra-relativistic electrons, the bulk Lorentz factor is negligible compared to the Lorentz factor of the electrons, so that photons from all azimuthal angles can be scattered into the observer's line of sight. Electrons with the mildly relativistic energies necessary for the production of optical/UV photons fall into the middle category, with polarisation fraction around 6%. Thus, observation of significantly higher linear polarisation would rule out the IC-CMB model and instead support a synchrotron origin for the jet's X-rays.

Unfortunately, the existing polarimetry for this jet has yielded contradictory results: Röser & Meisenheimer (1991) report a polarisation fraction of $p = 0.07 \pm 0.04$ based on ground-based data, while Thomson, Mackay & Wright (1993) report $p \approx 0.3$–0.4 using the not-yet-aberration-corrected Faint Object Camera (FOC) on HST. Also in other parts of the jet, the ground-based and FOC results are incompatible with each other. The ground-based data show the same polarisation fraction and flip in polarisation angle as radio observations of the radio "hot spot", which is identified with a strong jet-terminating shock (Meisenheimer & Heavens 1986; Meisenheimer et al. 1989; Meisenheimer, Yates & Röser 1997). Therefore, we deem the ground-based data to be more reliable and are inclined to ascribe the discrepancies predominantly to the low signal-to-noise ratio and the missing spherical aberration correction of the FOC data. Clearly, additional observations are needed to obtain a high-fidelity determination of the polarisation fraction, and hence clarify the X-ray emission mechanism.

4.3 Why is the jet morphology independent of wavelength even with two spectral components?

Even though the brightness profiles of this jet change from radio, infrared, optical to X-ray wavelengths, the locations of brightness peaks as well as their angular sizes are strikingly independent of wavelength (with the exception of B1, whose northern arc is brighter at infrared and higher frequencies, while the southern one is brighter at radio frequencies). This wavelength independence of this jet's morphology has been somewhat of a puzzle even before it was realised that there is more than one spectral component. For example, changing only the magnetic field strength, without varying the shape of the underlying electron population, should have a much stronger effect on the optical surface brightness than on that in the radio because the electron energy distribution is falling more steeply in the optically emitting range than at low energies. Nevertheless, the relative brightness changes from peak to peak are very similar in the radio and optical. The puzzle becomes even stronger with the addition of a second spectral component.

There are further jets showing a similar behaviour, with similar features at all wavelengths. However, others show strong peaks in one wavelength region (e.g., X-rays) without a correspondingly strong peak in another (e.g., radio), *i.e.*, peak shifts indicating a strongly changing spectral shape (*e.g.* PKS 1127$-$145 [Harris & Krawczynski 2006; Siemiginowska et al. 2007] and PKS 1150$+$497 [Sambruna et al. 2006]). There are also jets where some knots are like those in 3C 273 while others show peak shifts, again indicating a changing spectral shape, for example the jet in PKS 1136$-$135 (Uchiyama et al. 2007).

For 3C 273, we speculate (see §4.1 above) that the electron population responsible for the second, high-energy (UV/X-ray) emission component is fed from the population responsible for the optical synchrotron emission, and perhaps even caused by the same process, albeit in different volumes. By contrast, jets such as PKS 1127$-$145 may have a different X-ray emission mechanism, a different mechanism accelerating the X-ray emitting particles, or if the acceleration is related to velocity shear, differences in their flow patterns — though one should bear in mind that the jet lengths and resolved linear scales differ by large factors between these jets (Harris & Krawczynski 2006).

4.4 Nature of "optical extensions" to the jet

Observations at optical wavelengths up to 300 nm show several "extensions" to the jet, whose nature and relation to the jet material has remained elusive. Especially the "southern extension" S extending towards the southeast from region A had been speculated to be related to the jet, both due to its location at the onset of the jet, and because of its very blue SED between 620 and 300 nm (see Jester et al. 2001, Figures 1–3). Comparing the optical and ultraviolet images (Fig. 1), at 150 nm the extensions are conspicuous by their absence. As the appearance of the jet itself is not significantly different at 150 nm from that at longer or shorter wavelengths, this means that it is unlikely that any of the extensions consist of the same material and emit by the same mechanism as the jet itself. Since the SED of the quasar itself extends well beyond 150 nm, too, scattered quasar light is also ruled out as their origin. Instead, they are most likely unrelated galaxies.

5 SUMMARY

We have used the ACS/SBC on board *HST* with the `F150LP` filter to image the jet in 3C 273 at 150 nm with the highest possible resolution. Our observations show a close agreement of the jet morphology with that at longer wavelengths (Fig. 1); the "optical extensions" to the jet, however, are undetected at 150 nm, and we therefore believe that they are unrelated galaxies and not connected to the jet. The spectral energy distributions (Fig. 2) show that the spectral energy density at 150 nm lies above that at 300 nm in all parts of the jet. The far-UV flux is compatible with the extrapolation of the 0.5–8 keV X-ray flux and spectral index towards lower energies (Figs. 2 and 3). This lends strong support to a common origin of the jet's UV and X-ray emission. This high-energy component is distinct from the low-energy component responsible for the radio emission. The observed rise of the spectral energy density between 300 and 150 nm means that the high-energy spectral component does not cut off between 300 nm and the *Chandra* X-ray band. This confirms that part of the jet's emission also at longer wavelengths (620 and 300 nm) is already due to the same spectral component as the X-ray emission (compare Uchiyama et al. 2006).

In the X-ray brightest jet regions, (A, B1 and B2), the optical emission is even *dominated* by the high-energy component, and not by the low-energy component accounting for the optical emission in most of the jet. Thus, in these regions, optical polarimetry is equivalent to X-ray polarimetry. A model explaining the high-energy component as beamed inverse-Compton scattered cosmic microwave background (BIC) photons predicts a low degree of linear polarisation for the optical/UV emission (Y. Uchiyama & P. Coppi, *in prep.*). Therefore, observing a high degree of polarisation in these regions would rule out the BIC model for this jet's X-rays. The existing polarimetry of 3C 273 (Röser & Meisenheimer 1991; Thomson et al. 1993) has yielded contradictory results, and we have applied to perform additional polarimetric observations with HST/WFPC2.

In the broader context, it will be important to assess how common it is for the X-ray component to reach into the optical/UV region. *Spitzer* observations show similar SEDs as in 3C 273's region A in at least one knot of the jet in PKS 1136$-$135 (Uchiyama et al. 2007). However, given that 3C 273 shows a rise in the SED towards 150 nm, observations of further jets at this wavelength are an alternative route to assess in which jets the X-ray spectral component reaches down to the optical/UV region. This will enable the identification of further jets in which optical polarimetry can determine the X-ray emission mechanism. In cases where the X-rays are generated by the BIC mechanism, the low-energy end of the electron energy distribution can be studied directly in this wavelength region, while the corresponding radio synchrotron emission emerges at inaccessibly low frequencies. Thus, whether synchrotron or inverse-Compton emission, the low-energy end of the underlying particle energy distribution can be studied directly around 150 nm.

ACKNOWLEDGEMENTS

We are grateful to John Biretta for essential advice in planning these observations, to the staff of the STScI Helpdesk for their dedicated responses to our requests during the analysis, and to the anonymous referee for valuable comments. This work was initiated at the Fermilab Particle Astrophysics Center with support from the U.S. Department of Energy under contract No. DE-AC02-76CH03000. Support for HST GO program #9814 at Fermilab was provided by NASA through a grant from the Space Telescope Science Institute, which is operated by the Association of Universities for Research in Astronomy, Inc., under NASA contract NAS 5-26555. This research has made extensive use of NASA's Astrophysics Data System Bibliographic Services.

REFERENCES

Celotti A., Ghisellini G., Chiaberge M., 2001, MNRAS, 321, L1
Fossati G., Maraschi L., Celotti A., Comastri A., Ghisellini G., 1998, MNRAS, 299, 433
Hardcastle M. J., 2006, MNRAS, 366, 1465
Harris D. E., Krawczynski H., 2006, ARA&A, 44, 463
Jester S., Harris D. E., Marshall H. L., Meisenheimer K., 2006, ApJ, 648, 900
Jester S., Röser H.-J., Meisenheimer K., Perley R., 2002, A&A, 385, L27
Jester S., Röser H.-J., Meisenheimer K., Perley R., 2005, A&A, 431, 477
Jester S., Röser H.-J., Meisenheimer K., Perley R., Conway R. G., 2001, A&A, 373, 447
Katz-Stone D. M., Rudnick L., Anderson M. C., 1993, ApJ, 407, 549
Marshall H. L., et al., 2001, ApJ, 549, L167
Marshall H. L., et al., 2005, ApJS, 156, 13
Meisenheimer K., Heavens A. F., 1986, Nature, 323, 419
Meisenheimer K., Röser H.-J., Hiltner P. R., Chini R., Perley R. A., Yates M. G., Longair M. S., 1989, A&A, 219, 63
Meisenheimer K., Yates M. G., Röser H.-J., 1997, A&A, 325, 57
Munn J. A., et al., 2004, AJ, 127, 3034
Pavlovsky C., et al., 2006, ACS Instrument Handbook, Version 7.0. STScI, Baltimore
Pei Y. C., 1992, ApJ, 395, 130
Rieger F. M., Duffy P., 2004, ApJ, 617, 155
Röser H.-J., Meisenheimer K., 1991, A&A, 252, 458
Röser H.-J., Meisenheimer K., Neumann M., Conway R. G., Perley R. A., 2000, A&A, 360, 99
Sambruna R. M., Gambill J. K., Maraschi L., Tavecchio F., Cerutti R., Cheung C. C., Urry C. M., Chartas G., 2004, ApJ, 608, 698
Sambruna R. M., Gliozzi M., Donato D., Maraschi L., Tavecchio F., Cheung C. C., Urry C. M., Wardle J. F. C., 2006, ApJ, 641, 717
Sambruna R. M., Maraschi L., Tavecchio F., Urry C. M., Cheung C. C., Chartas G., Scarpa R., Gambill J. K., 2002, ApJ, 571, 206
Sambruna R. M., Urry C. M., Tavecchio F., Maraschi L., Scarpa R., Chartas G., Muxlow T., 2001, ApJ, 549, L161
Schlegel D. J., Finkbeiner D. P., Davis M., 1998, ApJ, 500, 525
Siemiginowska A., Stawarz Ł., Cheung C. C., Harris D. E., Sikora M., Aldcroft T. L., Bechtold J., 2007, ApJ, 657, 145
Stawarz Ł., Ostrowski M., 2002, ApJ, 578, 763
Stawarz Ł., Sikora M., Ostrowski M., Begelman M. C., 2004, ApJ, 608, 95
Tavecchio F., Maraschi L., Sambruna R. M., Urry C. M., 2000, ApJ, 544, L23
Thomson R. C., Mackay C. D., Wright A. E., 1993, Nature, 365, 133
Uchiyama Y., et al., 2006, ApJ, 648, 910
Uchiyama Y., et al., 2007, ApJ, 661, 719
Worrall D. M., Birkinshaw M., Hardcastle M. J., 2001, MNRAS, 326, L7
Zacharias N., Urban S. E., Zacharias M. I., Wycoff G. L., Hall D. M., Monet D. G., Rafferty T. J., 2004, AJ, 127, 3043

APPENDIX A: FLUXES FOR ALL JET REGIONS

This appendix gives fluxes for all jet regions collated from previous works (Jester et al. 2001, 2005, 2006; Uchiyama et al. 2006) and as plotted in Figure 2 in a single Table A1 for future reference. The apertures used for the regions are those shown in Figure 1 of Jester et al. (2006).

Table A1. Flux densities for all regions of the 3C273 jet. Original references by frequency: $8.33 \times 10^9, 1.5 \times 10^{10}, 2.25 \times 10^{10}$ Hz (VLA) and 1.87×10^{14} Hz (HST NIC2) from Jester et al. (2005); 5.23 and 8.45 $\times10^{13}$ Hz (*Spitzer* IRAC) from Uchiyama et al. (2006); 4.85×10^{14} and 10^{15} Hz (HST WFPC2 `F622W` and `F300W`) from Jester et al. (2001); 1.86×10^{15} Hz (HST ACS/SBC) from this work; 2.42×10^{17} Hz (*Chandra* ACIS-S) from Jester et al. (2006).

Frequency [Hz]	f_ν [Jy]	σ_f [Jy]	f_ν [Jy]	σ_f [Jy]	f_ν [Jy]	σ_f [Jy]
	Region					
	A		B1		B2	
8.33×10^{9}	0.0905	0.0001	0.0692	8.2×10^{-5}	0.105	0.00011
1.5×10^{10}	0.0589	5.1×10^{-5}	0.0419	4.1×10^{-5}	0.069	5.9×10^{-5}
2.25×10^{10}	0.0385	3.8×10^{-5}	0.0306	3.2×10^{-5}	0.0508	4.6×10^{-5}
5.23×10^{13}	4.5×10^{-5}	1×10^{-5}	3.5×10^{-5}	1.2×10^{-5}	3.62×10^{-5}	8.1×10^{-6}
8.45×10^{13}	2.7×10^{-5}	…	1.5×10^{-5}	2.6×10^{-6}	2.88×10^{-5}	…
1.87×10^{14}	1.13×10^{-5}	1.2×10^{-8}	4.9×10^{-6}	8.3×10^{-9}	1.02×10^{-5}	9.9×10^{-9}
4.85×10^{14}	4.93×10^{-6}	1.2×10^{-8}	1.83×10^{-6}	8.2×10^{-9}	3.86×10^{-6}	9.8×10^{-9}
1×10^{15}	3.2×10^{-6}	1.7×10^{-8}	9.73×10^{-7}	1.2×10^{-8}	1.88×10^{-6}	1.3×10^{-8}
1.86×10^{15}	2.03×10^{-6}	1.1×10^{-7}	6.26×10^{-7}	3.7×10^{-8}	1.47×10^{-6}	7.9×10^{-8}
2.42×10^{17}	4.65×10^{-8}	5.4×10^{-10}	1.09×10^{-8}	2.5×10^{-10}	2×10^{-8}	3.3×10^{-10}
	B3		C1		C2	
8.33×10^{9}	0.0508	7.8×10^{-5}	0.101	0.00012	0.205	0.00019
1.5×10^{10}	0.0348	4.5×10^{-5}	0.067	6.9×10^{-5}	0.134	0.00012
2.25×10^{10}	0.0236	3.3×10^{-5}	0.0488	5.3×10^{-5}	0.0971	8.6×10^{-5}
5.23×10^{13}	1.28×10^{-5}	2.9×10^{-6}	9.8×10^{-5}	1.1×10^{-5}	8.9×10^{-5}	1.2×10^{-5}
8.45×10^{13}	1.02×10^{-5}	…	4.6×10^{-5}	…	4.6×10^{-5}	…
1.87×10^{14}	4.84×10^{-6}	6.2×10^{-9}	1.08×10^{-5}	8.4×10^{-9}	1.81×10^{-5}	9.9×10^{-9}
4.85×10^{14}	1.37×10^{-6}	5.9×10^{-9}	2.93×10^{-6}	7.9×10^{-9}	3.93×10^{-6}	9×10^{-9}
1×10^{15}	5.07×10^{-7}	8.1×10^{-9}	1.16×10^{-6}	1.1×10^{-8}	1.28×10^{-6}	1.2×10^{-8}
1.86×10^{15}	4.39×10^{-7}	2.8×10^{-8}	6.57×10^{-7}	3.9×10^{-8}	7.23×10^{-7}	4.2×10^{-8}
2.42×10^{17}	3.41×10^{-9}	1.4×10^{-10}	4.85×10^{-9}	1.6×10^{-10}	6.25×10^{-9}	1.8×10^{-10}
	D1		D2H3		H2	
8.33×10^{9}	0.283	0.0003	0.836	0.00068	1.33	0.0013
1.5×10^{10}	0.182	0.00018	0.516	0.00041	0.782	0.00074
2.25×10^{10}	0.131	0.00013	0.357	0.00028	0.52	0.00048
5.23×10^{13}	1.54×10^{-4}	…	1.61×10^{-4}	…	8.7×10^{-5}	1.2×10^{-5}
8.45×10^{13}	8×10^{-5}	…	1.4×10^{-4}	…	4.1×10^{-5}	…
1.87×10^{14}	2.17×10^{-5}	9.5×10^{-9}	4×10^{-5}	1.3×10^{-8}	6.97×10^{-6}	9.4×10^{-9}
4.85×10^{14}	3.56×10^{-6}	8×10^{-9}	7.68×10^{-6}	1.1×10^{-8}	1.29×10^{-6}	9×10^{-9}
1×10^{15}	1.09×10^{-6}	1×10^{-8}	2.54×10^{-6}	1.4×10^{-8}	4.59×10^{-7}	1.3×10^{-8}
1.86×10^{15}	6.79×10^{-7}	4×10^{-8}	1.39×10^{-6}	7.5×10^{-8}	2.88×10^{-7}	2×10^{-8}
2.42×10^{17}	5.16×10^{-9}	1.7×10^{-10}	7.82×10^{-9}	2×10^{-10}	1.3×10^{-9}	8.6×10^{-11}